Electrochemical behavior of electrodeposited nanoporous Pt catalysts for the oxygen reduction reaction

Article

Electrochemical Behavior of Electrodeposited Nanoporous Pt Catalysts for the Oxygen Reduction Reaction

Bart Geboes, Jon Ustarroz, Kadir Sentosun, Hans Vanrompay, Annick Hubin, Sara Bals, and Tom Breugelmans

ACS Catal., **Just Accepted Manuscript** • DOI: 10.1021/acscatal.6b00668 • Publication Date (Web): 18 Jul 2016

Electrochemical Behavior of Electrodeposited Nanoporous Pt Catalysts for the Oxygen Reduction Reaction

Bart Geboes,*,†,‡ Jon Ustarroz,‡ Kadir Sentosun,¶ Hans Vanrompay,¶ Annick Hubin,‡ Sara Bals,¶ and Tom Breugelmans*,†,‡

†*University of Antwerp, Research Group Advanced Reactor Technology, Universiteitsplein 1, 2610 Antwerpen, Belgium*

‡*Vrije Universiteit Brussel, Research Group Electrochemical and Surface Engineering, Pleinlaan 2, 1050 Brussels, Belgium*

¶*University of Antwerp, Research Group Electron Microscopy for Materials Science, Groenenborgerlaan 171, 2020 Antwerpen, Belgium*

E-mail: bart.geboes@uantwerpen.be; tom.breugelmans@uantwerpen.be

Abstract

Nanoporous Pt based nanoparticles (NP's) are promising fuel cell catalysts due to their high surface area and increased electrocatalytic activity towards the ORR. In this work a direct double-pulse electrodeposition procedure at room temperature is applied to obtain dendritic Pt structures (89 nm diameter) with a high level of porosity (ca. 25%) and nanopores of 2 nm protruding until the center of the NP's. The particle morphology is characterized using aberration-corrected high angle annular dark field scanning transmission electron microscopy (HAADF-STEM) and electron tomography (ET) combined with field emission scanning electron microscopy (FESEM) and macroscopic electrochemical measurements to assess their activity and stability towards the

ORR. Macroscopic determination of the active surface area through hydrogen UPD measurements in combination with FESEM and ET showed that a considerate fraction of the active sites inside the pores of the low overpotential NP's were accessible to oxygen species. As a result of the accessibility of the active sites inside the nanopores, up to a 9 fold enhancement of the Pt mass corrected ORR activity at 0.85 V vs. RHE was observed at the highly porous structures. After successive potential cycling upwards to 1.5 V vs RHE in a deaerated $HClO_4$ solution a negative shift of 71 mV in half-wave potential occurred. This decrease in ORR activity could be correlated to the partial collapse of the nanopores, visible in both the EASA values and 3D ET reconstructions.

Keywords

Fuel Cell, Electrocatalyst, ORR, Nanoparticle, Nanoporous, Stability, Electron Tomography

1 Introduction

Polymer electrolyte membrane fuel cells (PEMFC) are a promising part of the future sustainable energy cycle. However, the high capital cost of PEMFC's compared to conventional electricity production impedes their widespread implementation.[1,2] The high Pt loading needed to achieve sufficient reaction rates at the cathode side is a result of the sluggish oxygen reduction reaction (ORR) kinetics. Over the past decade, the majority of investigated strategies to improve these ORR kinetics include the tuning of metal-support interactions[3–5] and alloying Pt with less noble transition metals (Co, Cu, Ni).[6–8] Despite the recent activity increments of bimetallic catalysts of up to six times compared to pure Pt, retaining the Pt mass based activity over time remains a major barrier.[9] Recently, nanoporous Pt based nanoparticles (NP's) with electrocatalytic activity towards the ORR have been the subject of several studies.[9–12] Although no consensus has been obtained until this point, the increase in ORR

activity is generally attributed to a combination of effects: (i) higher active site residence time attributed to a confinement effect within the nanopores,[13–17] (ii) an increase in surface area to volume ratio[18] and (iii) a smaller fraction of low-coordinated atoms.[19,20]

Despite the observed activity increase in nanoporous Pt based NP's, several degradation mechanisms in fuel cell relevant conditions have been reported by Baldizzone et. al.[10] Gan et. al. described a size-dependent rapid drop in intrinsic catalytic activity as a result of Ni dissolution and related porosity formation.[9] A profound understanding of the morphology-activity relationship is thus imperative to design more active and stable PEMFC catalysts. The high amount of control on particle morphology needed for this goal can be achieved using electrodeposition. It is one of the most popular single-step NP synthesis procedures as it ensures electrical contact between the NP and the substrate, and offers several easily controllable parameters (deposition potential, time, temperature and electrolyte composition).[21,22] However, the disadvantage of electrodeposition procedures is the relatively broad size distribution generally obtained. The main cause for this is believed to be the diffusional coupling between neighboring metal particles on the electrode surface.[23] In addition, the formation of new NP nuclei during the entire deposition procedure[24] and possible Ostwald ripening[25,26] further influence the size distribution broadening. To overcome these problems a potentiostatic double pulse technique was developed by the groups of Penner and Plieth.[23,24] Nuclei formation and growth are separated in time by first applying a short nucleation pulse of high overpotential, followed by longer growth pulse of low overpotential. Relatively monodisperse metal NP's have since been synthesized on several occasions.[22,27–29]

The use of electrodeposition for catalyst application in PEMFC's holds several advantages over conventional chemical methods such as impregnation, spraying and evaporative deposition. It can be applied directly on the MEA (even on more complex geometries), decreasing the number of processing steps and thus cost.[30] No expensive equipment is needed such as with vacuum deposition or sputtering techniques.[31] Most importantly, Pt is only deposited in regions with ionic and electronic conductivity. In chemical techniques where

the catalyst ink is applied on the membrane in the final step, 30 to 50 % of the catalyst has been reported to be inactive in the MEA.[32,33] This combination of effects thus renders electrodeposition a viable and cost effective technique for MEA fabrication.

According to recent literature, nanoporosity is generally achieved by preferential leaching of the least noble metal (e.g. Ni, Co, Pd) from bimetallic NP's. The formation of a nanoporous structure as a result of the (electro)chemical dealloying is attributed to a nanoscale Kirkendall effect.[8,34–37] This vacancy mediated diffusion mechanism in binary metal NP's is driven by the faster interdiffusion of one element relative to the other. In our recent work the growth mechanism of dendritic porous Pt nanostructures through electrodeposition was investigated.[38] The morphology of the obtained nanostructures appeared to depend on the degree of coalescence and recrystallization of nanocluster aggregates, which in turn is influenced by the electrodeposition potential. At low overpotentials, a self-limiting growth mechanism may block the epitaxial growth of primary nanoclusters and results in loose dendritic aggregates. Nonetheless, to the best of our knowledge no direct double pulse electrodepostion procedure has been proposed to obtain nanostructured monometallic Pt NP's with pore sizes in the nm range.

In this work a direct double-pulse electrodeposition procedure at room temperature is applied to obtain nanoporous Pt structures. The particle morphology is characterized using aberration-corrected high angle annular dark field scanning transmission electron microscopy (HAADF-STEM) and electron tomography (ET) combined with field emission scanning electron microscopy (FESEM) and macroscopic electrochemical measurements to asses their activity and stability towards the ORR.

2 Experimental

2.1 Electrodeposition of porous Pt nanoparticles

Prior to every deposition, the glassy carbon electrode substrate (0.6 cm disk) was successively polished using 1 μm, 0.3 μm and 0.05 μm alumina powder (Struers) suspended in ultra pure water (18.2 MΩ cm, Merck MilliPore) to achieve a reproducible mirror like surface. Afterwards the electrode was successively sonicated in isopropanol (Acros, HPLC grade) and ultra pure water for 5 minutes. A double potentiostatic pulse procedure was used to deposit the porous Pt nanostructures directly on the glassy carbon electrode. An Autolab PGSTAT 302F potentiostat was used to apply the potentiostatic deposition pulse to a three electrode cell with a Ag/AgCl reference electrode and Pt wire counter electrode. The deposition solution consisted of 1 mM $H_2PtCl_6.6H_2O$ (Alfa Aesar, ACS grade) in 0.1 M KCl (Alfa Aesar, ACS grade). The pH of the deposition solution was adjusted by adding a 0.1 M KOH solution until pH reached 6. To obtain a higher surface coverage of the Pt nanostructures without losing the morphological control, the electrodes were rotated at 700 rpm during the deposition procedure using a Radiometer EDI-101 rotating disk electrode (RDE). For the high resolution HAADF-STEM and electron tomography (ET) measurements, identical deposition conditions were applied to TEM grids, taped to the inert glassy carbon RDE electrode assuring a good electrical connection.[39] The mass amount of the depositions was determined by stripping all Pt from the electrode surface using aqua regia. The stripping time was varied until no nanoparticles where visible on FESEM images and no electrochemical Pt response could be obtained using cyclic voltammetry. Pt stripping solutions were analyzed with a high resolution sector field ICP-MS (Element XR, Thermofisher Scientific, Bremen, Germany).

2.2 Microscopic characterization

SEM images were acquired using a FEI Quanta 250 FEG microscope operated at 20 kV and yielded the particle size distribution and coverage of the particle deposits. Aberration-corrected HAADF-STEM was used to image the detailed morphology of the nanoparticle structures with atomic scale structural information. Abberation corrected HAADF-STEM images were obtained using a FEI Titan 50-80 microscope operated at 300 kV. The Electron Tomography (ET) experiments were performed using a FEI Tecnai G2 and Tecnai Osiris microscope operated at 200 kV. A Fischione tomography holder (model 2020) was used and the tilt series were acquired over a tilt range of $\pm 74^{\circ}$ with a 3° increment. As working electrodes, carbon coated gold TEM grids from EMS (300 mesh, CF 300Au) were used. To measure porosity of the samples, a segmentation of the 3D reconstruction is required. During this segmentation, voxels were classified as Pt (V_{Pt}) or pores in the Pt particle. Next, the voxels corresponding to empty space were analyzed. The voxels that have connection with the exterior (V_e) were distinguished from the voxels that have no connection with the exterior and which therefore correspond to internal voids inside the Pt nanoparticle (V_i). In order to perform this analysis, each of the slices of the 3D reconstruction was analyzed using a dedicated algorithm developed in Matlab. Finally, the porosity P was defined using Equation 1 as the volume ratio between the pores that have a connection with the exterior V_e and the entire volume of the Pt nanoparticle.

$$P = \frac{V_e}{V_{Pt} + V_e + V_i} \tag{1}$$

2.3 Electrochemical characterization

Electrochemical active surface area (EASA) and ORR activity measurements were obtained in a fast screening reactor with four parallel electrochemical cells. These cells with a three electrode system using a Ag/AgCl reference electrode with a Luggin capillary and a Pt foil

counter electrode were connected to a multi channel Biologic VSP-300 potentiostat equipped with an analogue scan generator. All cells are equipped with a Radiometer EDI-101 rotator. A 0.1 M $HClO_4$ (Merck, Emsure) electrolyte solution was used which could be saturated with N_2 (99.999 %) or O_2 (99.996 %) prior to the measurements and the gas flow was directed as a blanket over the solution during the measurements.

3 Results and discussion

3.1 Direct electrodeposition of Pt NP's on glassy carbon disk electrodes

In contrast to conventional chemical methods to obtain NP's, electrodeposition processes can be monitored in-situ by recording the current (or potential) transients during the application of the potential (or current) pulses. Both the potential modulation and the current transients are shown in Figure 1. Prior to the electrochemical deposition, an anodic stripping potential of 1.0 V vs. Ag/AgCl is applied during 120 s to avoid spontaneous Pt deposition and to remove impurities from the electrode surface. The current response during this pretreatment step is minimal at only a few micro ampere indicating a clean substrate and the absence of oxidizable species. A double pulse deposition of Pt is carried out with a nucleation pulse (E_{nuc}) of -0.4 V for 50 s and a growth pulse (E_{gr}) of -0.1 V for 50s (dashed black lines). The other deposition procedure comprises a nucleation pulse of -0.6 V for 50 s and a growth pulse of -0.2 V for 100 s (solid black lines). These procedures are later referred to as low and high overpotential (η) deposits respectively. The discussed deposition procedures are selected on the basis of nanoporosity from a prior parameter study.

Care has to be taken while interpreting the current transients of both nucleation and growth pulses because the deposition is performed on a rotating disk electrode with a rotation rate of 700 rpm. Rotating the substrate appeared successful in obtaining higher surface coverage of NP's without substantially altering the NP morphology. Although no typical

current peak - characteristic of the 3D island growth mechanism - is always expected in the early stages of Pt deposition,[40] the i(t) transients differ from what has been shown previously for stagnant conditions. By rotating during the electrodeposition process, the diffusion of Pt ions to the electrode surface may not be the rate-determining factor, even if large overpotentials are applied. Therefore, the increasing current response in the nucleation phase for both low and high overpotential depositions is indicative of a mixed or kinetically controlled growing active surface area. It must be noted that Pt electrodeposition in the nucleation potential range occurs simultaneously with proton reduction reactions, catalyzed on the formed Pt surface. Therefore the obtained current response presents a convolution of both phenomena. This poses a problem when the mass of deposited Pt is calculated using the deposition charge. To decrease the extent of hydrogen reduction the acidity of the electrodeposition solution is lowered until pH 6. The higher current response in both nucleation and growth phase (-2.0 mA cm^{-2} compared to -1.5 mA cm^{-2}) of the high overpotential deposition can partly be explained by a greater extent of hydrogen reduction at this potential. The higer overpotential (increasing the $PtCl_6^{2-}$ reduction kinetics) in combination with the longer growth pulse results in a larger amount of Pt deposited on the substrate. This is verified by the stripping experiments, with 70.8 and 1.6 μg cm^{-2} of Pt on the high overpotential and low overpotential deposition respectively.

FESEM pictures are used to elaborate statistics of the particle distributions. Figure 2 shows an overview of the distribution of Pt NP's using the high (a) and low (b) overpotential procedure. The average particle size of the low overpotential deposition is 89 nm compared to 116 nm for the high overpotential procedure. This difference in average particle size is a result of longer growth time (100 s) in the latter procedure. The histograms obtained from the FESEM images of the low and high overpotential deposits are shown in Figure S1 (a) and (b) respectively. In both deposits a bimodal size distribution is found where a limited amount of smaller NP's around 10 nm in diameter were formed in addition to the larger deposits. Such a bimodal size distribution is common in electrodeposition even

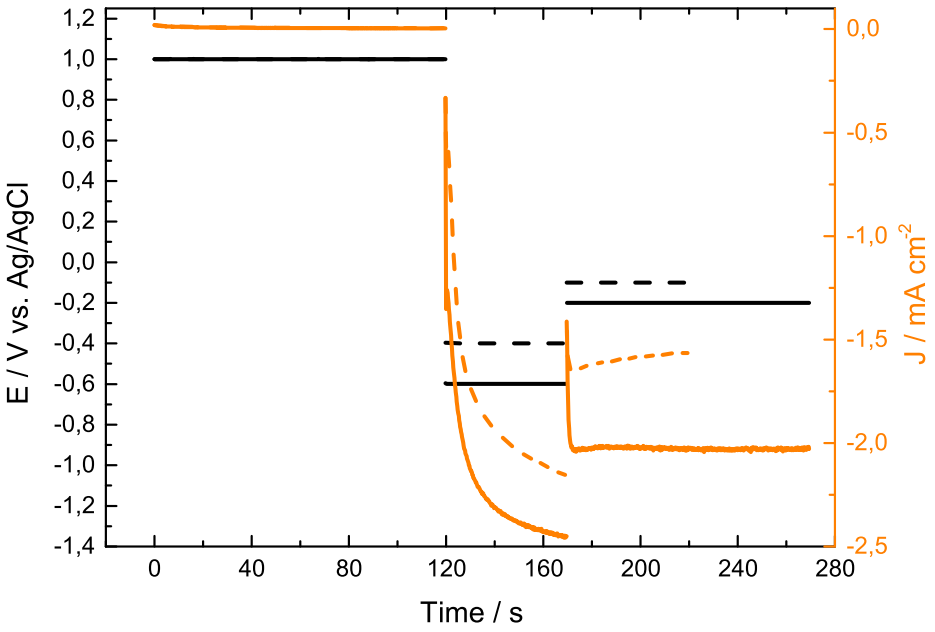

Figure 1: Chronoamperommetric current transients obtained for the electrodeposition of Pt on smooth glassy carbon substrates. The potential modulation (black lines) and current response (orange lines) are shown for the low (E_{nuc} = -0.4 V Vs. Ag/AgCl, dashed lines) and high (E_{nuc} = -0.6 V Vs. Ag/AgCl, solid lines) overpotenial samples.

when a double pulse procedure is used.[41,42] During the deposition, partial coalescence of some diffusion fields or physical coalescence upon growing islands could occur and would not imply complete inhibition of nucleation on the carbon surface.[40] Instead, this would only lead to a gradual decrease of the nucleation rate. The fraction of small NP's is limited to 3 % and 8 % in the low and high overpotential samples respectively. A clear difference in surface coverage is observed between both samples: the low η sample has only a coverage of 1.6 % whereas the high η sample covers 50 % of the glassy carbon surface. Such inversed trend in particle density and deposition overpotential corresponds to obeservations reported earlier.[38]

3.2 TEM characterization of as-electrodeposited nanostructures

In order to gain deeper insight into the 3D morphology of the electrodeposited nanostructures, HAADF-STEM tomography experiments were performed for both high (E_{nuc} -0.6 V, E_{gr} -0.2 V) and low overpotential (E_{nuc} -0.4 V, E_{gr} -0.1 V) deposits. A 3D visualization

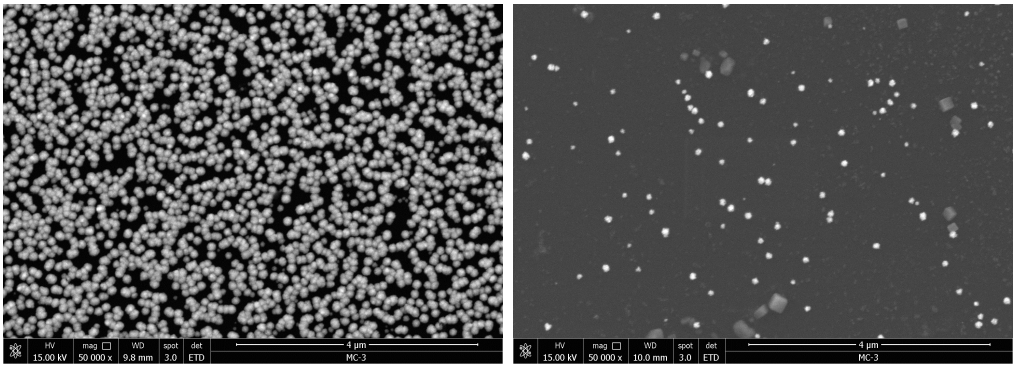

(a) (b)

Figure 2: FESEM pictures after the deposition of Pt on glassy carbon RDE electrodes using a nucleation potential of -0.6 V vs. Ag/AgCl (a) and -0.4 V vs. Ag/AgCl (b).

of the reconstruction obtained from a 115 nm high overpotential particle (corresponding to the average particle size that was determined by FESEM analysis) is presented in Figure 3 (a). It is clear that the surface area of the nanoparticles exhibits a dendritic morphology, which leads to an increased surface/volume ratio of the nanoparticle. However, a slice through the reconstruction, presented in Figure 3 (b) clearly reveals that the small channels inside the nanoparticle have mostly no connection to the outer surface. A 3D visualization of the reconstruction and a slice through the 3D data set of a low overpotential particle are presented in Figure 3 (c) and (d), respectively. The particle has a diameter of ca. 88 nm which corresponds to the average particle size calculated from FESEM images. Figure 3 (d) confirms the highly dendritic morphology which is present inside the nanoparticle. Quasi-spherical protuberance of ca. 2.5 nm are observed on the outer edges of the nanostructure highlighted with a circle, which are linked to the rest of the body by narrower necks depicted with an arrow. The highly dendritic morphology drastically increases the surface area of the low overpotential sample. High resolution HAADF-STEM images demonstrate that domains with different crystallographic orientations coexist within the same particle. The polycrystalline nature of the nanoparticle is confirmed by FFT patterns (shown in Figure S2), which is similar to the previously reported single pulse potentiostatic electrodeposition particles.[38]

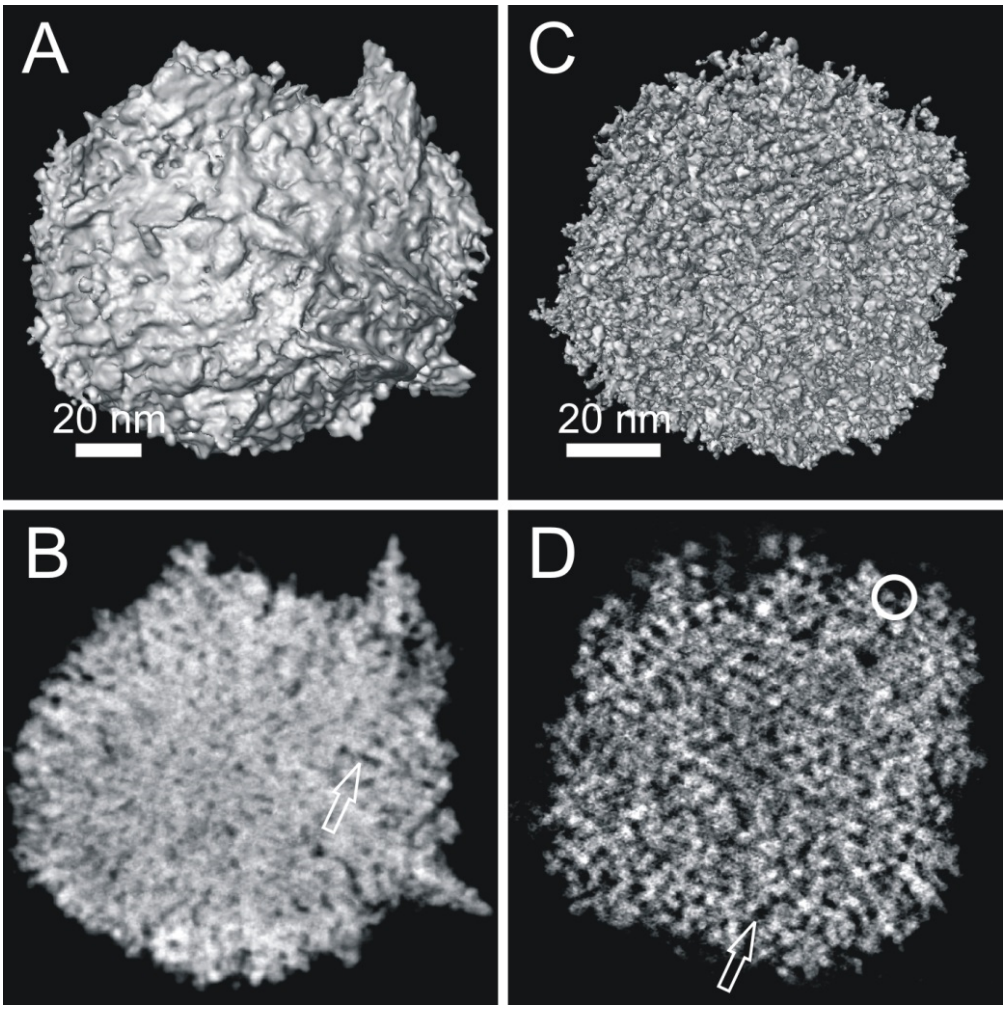

Figure 3: 3D visualization of the ET reconstruction and a slice through the 3D data set are depicted for -0.6 V high overpotential (a,b) and -0.4 V low overpotential particles (c,d), respectively. The dendritic morphology of the low overpotential particle can be clearly observed from the 3D visualization.

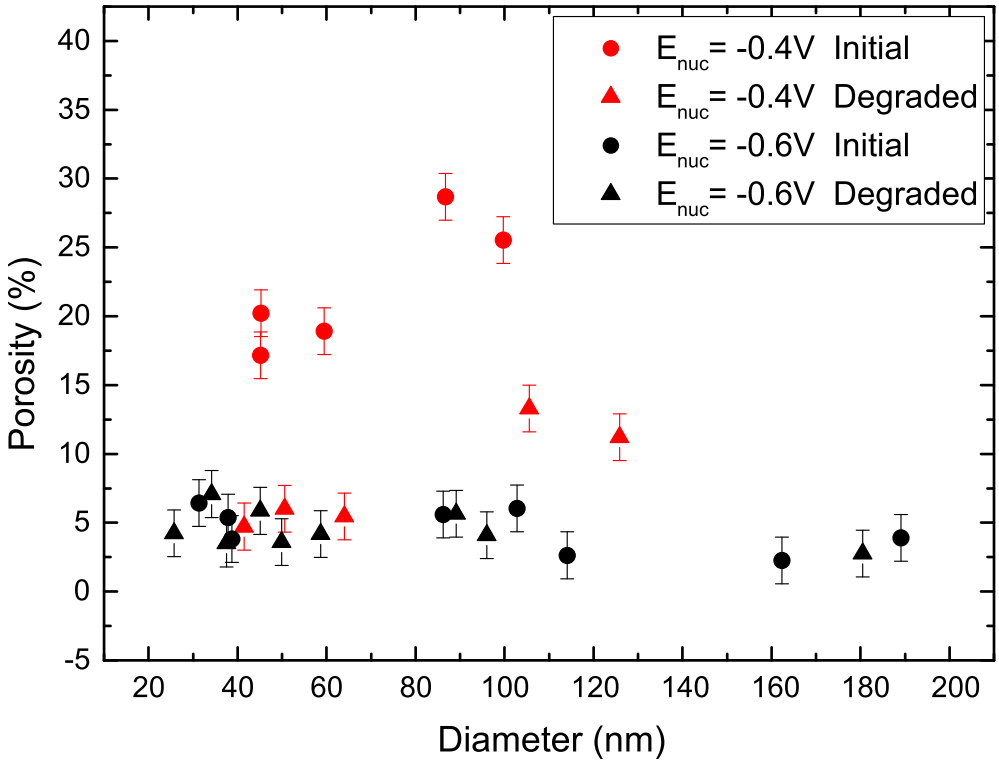

Figure 4: Porosity values calculated from the 3D tomography reconstruction for the as deposited low (red circles) and high overpotential catalysts (black circles). Porosity values after catalyst degradation using 600 potential cycles between 0.1 V and 1.5 V are shown for the low (red triangles) and high overpotential catalysts (black triangles).

The porosity extracted from the 3D reconstruction of several nanoparticles is plotted in function of particle size in Figure 4. The high overpotential catalyst has a porosity of ca. 5 % in the entire measurement range of particle size (black circles). The porosity in these particles is mainly formed through surface roughness while almost no internal pores are accessible. In the low overpotential particles a clear size dependency is visible (red circles). Care has to be taken when extrapolating the calculated porosities towards the entire electrode surface due to the local nature of the tomography measurements. Although with a porosity between 17 and 28 % there is a significant difference between all measured high overpotential catalyst particles.

3.3 Electrocatalytic ORR performance of nanoporous Pt nanostructures

Figure 5 shows the obtained cyclic voltammograms of the low (red line) and high overpotential (blue line) catalysts. In the cathodic scan between ca. 0.5 V–0.3 V and in the anodic scan between 0.3 V and 0.6 V the electrochemical double layer region is visible. The hydrogen adsorption/desorption peaks emerge in the region of 0.05V to 0.3V. The main characteristics of the peak are two well delineated sub-peaks in the adsorption region and three peaks in the desorption region. These separate H peaks and their cathodic counterparts are usually attributed to different forms of adsorbed H namely, strongly and weakly bound H. The relative amount of strongly adsorbed H ($0.25 <$ E vs. RHE < 0.4) is larger in the low overpotential porous catalyst, indicating a larger surface fraction of (100) and (111) facets compared to the high overpotential catalyst. The hydrogen adsorption peaks can be integrated to calculate the total charge passed during the adsorption process. The boundary conditions for determining the potential range of these peaks are the relative maxima in the double layer region and the onset of the hydrogen evolution. Both anodic and cathodic peak areas are indicated by the filled area in Figure 5. Through the weighted average coverage of the H atoms in polycrystalline Pt, the proportionality constant of $210 \mu C/cm^2$ is determined.[43–45]

Via this value the EASA can be calculated based on the charge amount of the hydrogen adsorption region.

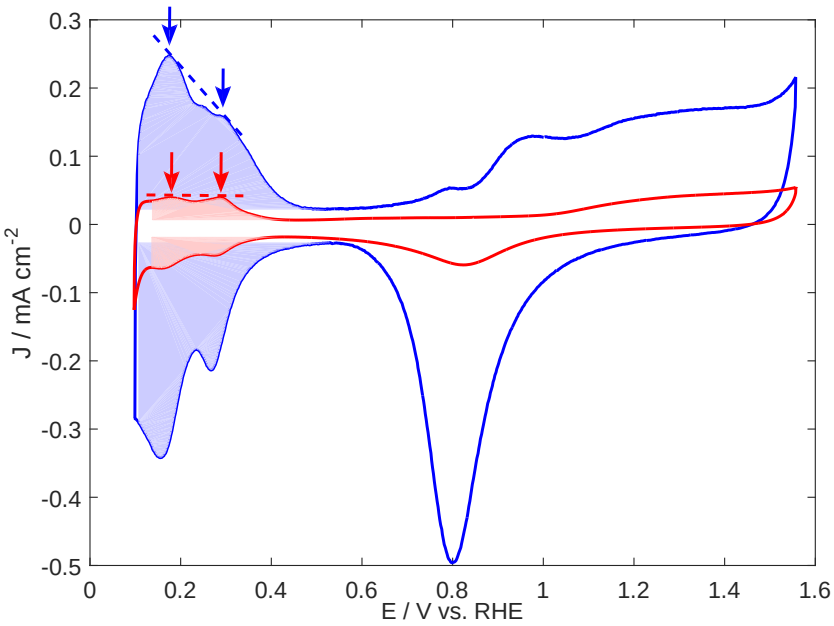

Figure 5: Cyclic voltammograms of the high (blue solid line) and low overpotential (red line) catalysts. Filled areas indicate the total charge passed during hydrogen underpotential deposition (HUPD), used to calculate roughness factor and EASA. Measurements conducted in nitrogen saturated 0.1 M $HClO_4$ solution without rotation at 298 K and 50 mV s^{-1}.

The roughness factors (R_f) obtained from the H UPD measurements of the low and high overpotential catalysts are 0.6 and 4.4 respectively (Table 1). This factor 7 increase for the high overpotential catalyst can be explained based on the higher surface coverage. Although the difference in surface coverage between both catalysts is much higher (factor 31). The substantial porosity of the low overpotential catalyst observed in ET measurements is likely to be the cause for the higher active surface area and corresponding roughness factor. This observation is confirmed when R_f is compared to the roughness factor based on FESEM analysis ($R_{f,SEM}$). This value is calculated by determining the geometric surface area for each imaged NP and extrapolated to the total electrode area. Here, it is postulated based on ET results of both deposits that all NP's have an oblate ellipsoid geometry where the

length of the z-axis (c) is 60% of the length of the x and y-axis (a). Volume and surface area are thus calculated as follows:

$$V = \frac{4}{3}\,\pi a^2 c \tag{2}$$

$$S = 2\,\pi a^2 \left(1 + \frac{(1-e^2)}{e}\,\mathrm{atanh}\,(e)\right) \qquad \text{with} \quad e = 1 - \frac{c^2}{a^2} \tag{3}$$

An underestimation of the SEM based roughness factor is attained for the high overpotential catalyst (1.8 compared to R_f of 4.4). Since the NP's imaged with FESEM and ET are not smoothly ellipsoidal (cf. spike formation in random directions) this underestimation with a factor 2 is plausible. When the same methodology is applied to the low overpotential particles, an underestimation with a factor 10 is calculated. Only the irregular shaped outer surface area of the NP's cannot explain the large deviation between H UPD and SEM based roughness factors. Where the 3D ET reconstructions show pores with an internal diameter of 2 nm propagating throughout the entire particle, they do not give direct information on the accessibility of active sites. Based on the prior observations it is concluded that active sites inside the nanopores of the low overpotential deposited structures are indeed accessible . Opposed to R_f, the EASA of solid NP's does depend on surface coverage and particle size since the surface-to-volume ratio of an ellipsoid depends on its diameter. Not only the smaller particle size and surface coverage relative to the HUPD charge, but also the porosity of 25 % lead to the factor 7 increase in EASA of the low overpotential catalyst. The value of 46.1 $m^2_{Pt}\ g^{-1}_{Pt}$ even competes with high surface area carbon supported fuel cell catalysts.[11,45–47]

Table 1: Calculated and experimental NP parameters derived from FESEM and electrochemical surface area measurements.

	High overpotential (E_{nuc} = -0.6 V)	Low overpotential (E_{nuc} = -0.4 V)
diameter (nm)	116	89
Surface coverage (%)	50	1.6
$R_{f,SEM}$ (-)	1.8	0.06
R_f (-)	4.4	0.6
EASA ($m^2_{Pt}\ g^{-1}_{Pt}$)	6.5	46.1

ORR activity measurements in this section are obtained by linear sweep voltammograms with scan rate of 5 mV s^{-1} using a rotating disk electrode. The potential is swept starting at 0.1 V vs. RHE in positive direction in order to avoid excessive H adsorption in the lower potential region. To check the influence of possible capacitive currents a blanc sweep obtained in a nitrogen saturated $HClO_4$ electrolyte solution is performed. The ORR sweeps are in their turn obtained after saturating the electrolyte solution with oxygen during a 15 minute window.

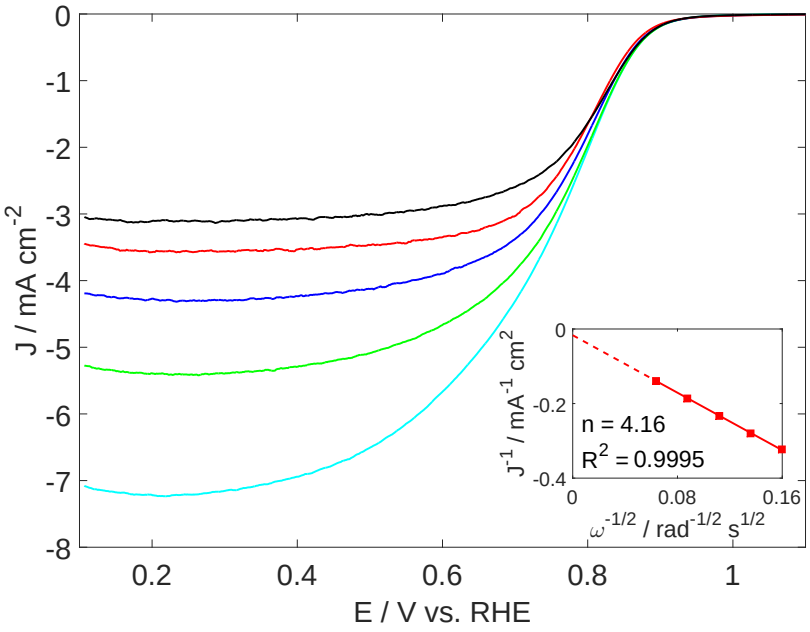

Figure 6: Linear sweep voltammograms recorded in the anodic direction on the high overpotential (-0.6 V vs. Ag/AgCl) catalyst during RDE rotation rates of 554, 816, 1322 and 2500 rpm. Koutecký-Levich analysis at 0.2 V vs. RHE plotted in inset. Measurements conducted in oxygen saturated 0.1 M $HClO_4$ solution at 298 K and 5 mV s^{-1}.

The linear sweep voltammogram obtained for the high overpotential catalyst at various rotation speeds is shown in figure 6. After a region with no activity between 1.3 V and 0.95 V the onset of the ORR initiates the kinetic region until ca. 0.85 V. The potential-current relationship is given by the Butler-Volmer equation due to the kinetic control of the ORR. The mixed kinetic and diffusion region spans until ca. 0.5 V, where it transfers into the diffusion limited region. The measured current plateau is a result of the fixed RDE

rotation rate, delivering oxygen at a constant rate to the electrode surface. The linear sweep voltammogram of the low overpotential catalyst shows a similar course to Figure 6 with a single well-formed reduction wave. Despite the lower surface coverage of the low overpotential deposition, the comparable diffusion limited current density for both catalysts is an indication that sufficient coverage is obtained to avoid divergent activity measurements.[47]

$$\frac{1}{I} = \frac{1}{I_k} + \frac{1}{B\omega^{1/2}} \tag{4}$$

$$B = 0.62nFAD_{0_2}^{2/3}\nu^{-1/6}C_{O_2} \tag{5}$$

The Koutecký-Levich analysis at 0.2 V vs. RHE is shown in the inset. The calculated number of exchanged electrons is 4.16 and 4.13 for the high (-0.6 V) and low overpotential (-0.4 V) catalyst respectively. Both values are close to each other and (within the literature scatter for oxygen concentration and diffusion coefficient values) in line with most reports in literature. The oxygen reduction thus follows the $4e^-$ pathway on both the solid and the nanoporous catalysts. Unlike high surface area carbon supported FC catalysts, the model electrodes prepared in this work do not suffer from diffusional limitations in the porous catalyst layer on the glassy carbon substrate. Since detachment of the electrodeposited NP's during RDE measurements did not appear to be a problem, no perfluorosulfonic acid (PFSA) binder was used when preparing the electrodes. The Koutecký-Levich equation (Equation 4) could thus be utilized without an extra diffusional term to incorporate film porosity.[48]

The ORR activity of both catalysts is assessed using RDE linear sweep voltammetry at 298 K in O_2 saturated $HClO_4$. Several activity measures are displayed in Figure 7: (a) J_K, kinetic current density based on geometric electrode area; (b) $J_{K,SA}$, electrochemical surface area corrected current density and (c) $J_{K,MA}$, mass based current density. Activity is determined at 0.8 V and 0.85 V vs. RHE after ohmic drop compensation. At first sight, the high overpotential Pt structures exhibit higher activity at both 0.8 V and 0.85 V, though

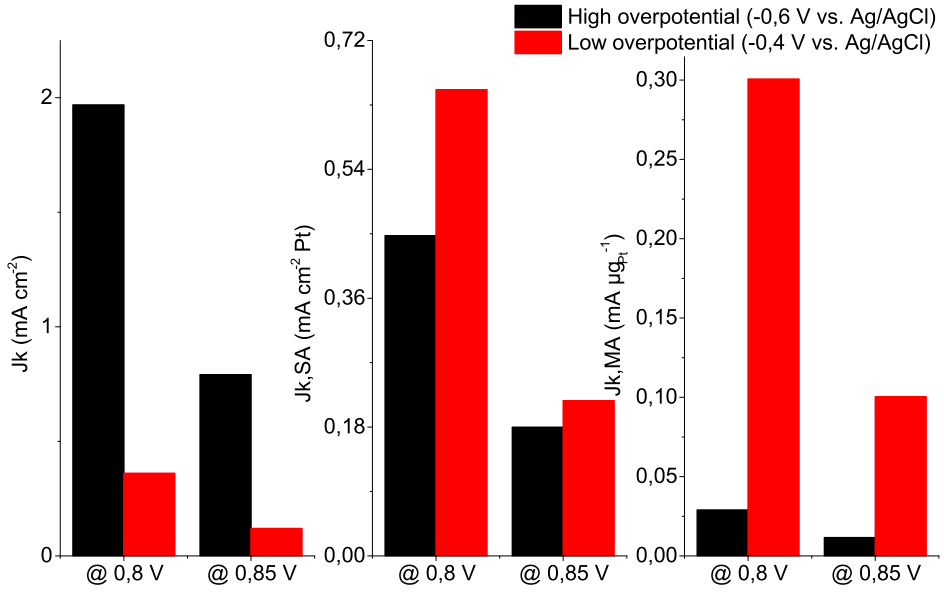

Figure 7: Comparison of ORR activity between high and low overpotential nanostructures at 0.8 and 0.85 V vs. RHE. The kinetic current density J_k, specific current density $J_{k,EASA}$ and Pt mass based current density $J_{k,m}$ are shown for both catalysts. Measurements performed in 0.1 M $HClO_4$ at 298 K with a rotation rate of 1322 rpm.

when the active surface area is taken into account the porous catalyst shows a higher activity compared to the solid reference catalyst of 46% and 21% at 0.8 V and 0.85 V respectively. Both platinum lattice contractions and alternate crystallographic orientation possibly lie at the basis of this activity enhancement.[11,49,50] The mass amount of the platinum deposits cannot be directly evaluated using the chronoamperometric curves, since simultaneous proton reduction is essential in the growth mechanism to obtain nanoporous structures. Instead, the Pt mass determined by the ICP stripping was used to calculate the mass based activity. The resulting mass based activity reveals a 10 and 9 fold increase on the porous catalyst at 0.8 V and 0.85 V respectively. The even higher mass based activity increase can be described by the nanoporous nature of the low overpotential catalyst. At the average particle diameters at hand in both catalysts (ca. 100 nm) the porous morphology has a significant effect on the amount of platinum within a NP. Although the mass based kinetic current density is significantly increased by introducing nanopores in the electrodeposited catalyst, the activity of commercial carbon supported fuel cell catalysts is not yet reached (see Fig. S3). When

the reduction wave of the low overpotential catalyst at 1322 rpm is compared to that of a 20 wt% Vulcan XC72 supported catalyst from Johnson Matthey, a shift in half-wave potential of ca. 30mV is observed. However, we note that care has to be taken when directly comparing these model electrodes to high surface area carbon supported catalysts.

3.4 Electrocatalytic stability of highly porous Pt nanostructures

To investigate the stability towards the ORR under harsh fuel cell start-up conditions 2000 oxidation/reduction cycles in a deaerated 0.1M $HClO_4$ electrolyte solution between 0.1 V and 1.5 V are applied using a scan rate of 50 mV s^{-1}. Because the HUPD region is integrated in the potential window a continuous monitoring of the active surface area becomes possible. The resulting roughness factor lapse is shown in Figure 8(a) and (b) for the high and low overpotential catalysts respectively. Roughness factors are determined based on the HUPD adsorption as well as desorption peaks. Both nanostructures undergo a drastic decrease in surface area of 50.4% and 80.3% for the solid and porous catalyst respectively. A 3D electron tomography reconstruction of the low overpotential catalyst is performed after 600 oxidation/reduction cycles (Figure 8C, left hand side). A substantial collapse of the nanopores is clearly visible in the 3D particle reconstruction. The porosity of both as prepared and degraded NP's in function of particle diameter is shown in Figure 4. Porosity of the as prepared low overpotential catalyst (red circles) around 100 nm is in the range of 25 %. After degradation through potential cycling (red triangles) the porosity is diminished to ca. 10 %. The low overpotential catalyst only has a porosity of ca. 5 % before and after degradation (black circles and black triangles respectively) over the entire range of measured diameters. It appears that a semi-stable morphology is obtained. This is an indication that the collapse of nanopores is not a part of the degradation mechanism for the low overpotential catalyst. The relatively large particle size and low coverage prevent agglomeration which is not observed in the degraded catalysts. The plateau with constant R_f values in Figure 8 (a) starting after ca. 1000 cycles supports this hypothesis.

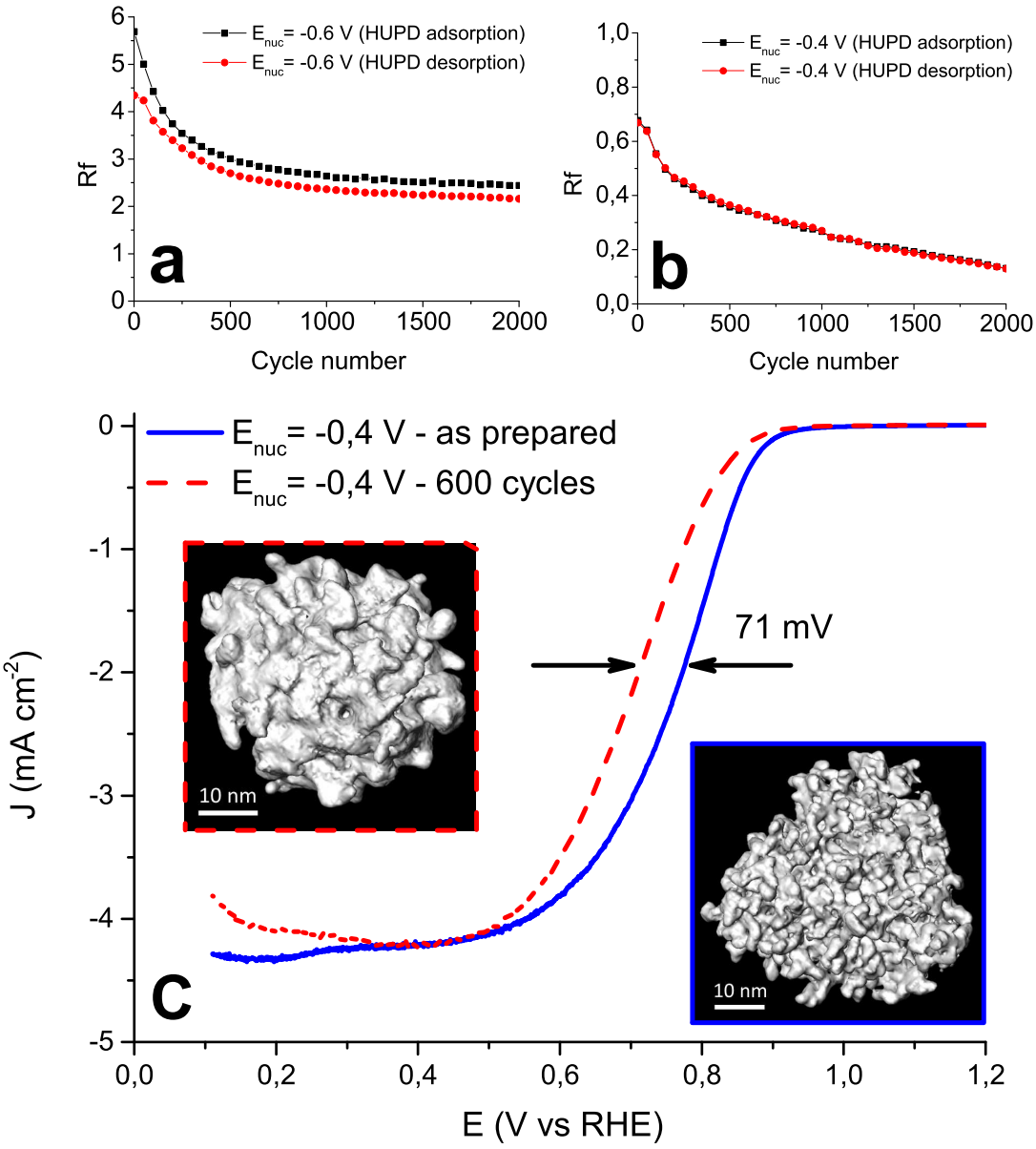

Figure 8: Electrochemical surface area evolution depicted through the roughness factor (R_f) of the high (a) and low overpotential (b) nanostructures. Accelerated stress tests consisted of successive potential cycling between 0.1 and 1.5 V vs. RHE in deaerated 0.1 M $HClO_4$ solution, relevant for fuel cell start-up cycles. (c) Shift in linear sweep voltammogram half-wave potential after 600 oxidation-reduction cycles in deaerated electrolyte solution.

The ORR reduction activity of the porous as prepared catalyst and after an accelerated degradation test of 600 oxidation/reduction cycles is shown in Figure 8C. The single reduction wave has undergone a negative shift in half-wave potential of 71 mV. This relatively large activity decrease is caused by multiple degradation mechanisms. First of all the collapse of the nanopores induces a severe change in morphology, reducing the lattice strain in the nanostructure and altering the accessible crystal plains. In addition, the extent of platinum dissolution as a result of the positive scan boundary could further decrease ORR activity.[10]

4 Conclusions

Nanoporous Pt structures with an average diameter of 89 nm and 2 nm pore sizes were successfully synthesized via the proposed double pulse electrodeposition procedure on smooth glassy carbon substrates. Macroscopic EASA determination using HUPD measurements in combination with FESEM and ET showed that a considerate fraction of the active sites inside the porosities of the low overpotential NP's were accessible to oxygen species. As a result of the accessibility of the active sites inside the nanopores, an enhancement of the electrochemical surface area corrected ORR activity was observed at the highly porous structures. The higher amount of low-coordinated sites in these nanostructures or the presence of a lattice effect could possibly cause this increase in surface based activity. The effect on the mass corrected activity was even more pronounced with a factor 10 increase at 0.8 V vs. RHE compared to non-porous deposited Pt NP's. The stability of the Pt NP's was evaluated using an accelerated stress test relevant to fuel cell start-up conditions. After successive potential cycling upwards to 1.5 V vs RHE in a deaerated $HClO_4$ solution a negative shift of 71 mV in half-wave potential occurred. This decrease in ORR activity was correlated with the partial collapse of the nanopores confirmed by macroscopic HUPD measurements and nanoscale 3D reconstruction electron tomography.

Acknowledgement

The Quanta 250 FEG microscope of the Electron Microscopy for Material Science group at the University of Antwerp was funded by the Hercules foundation of the Flemish Government. The authors acknowledge financial support from the Fonds Wetenschappelijk Onderzoek in Flanders (FWOAL708). S.B. acknowledges financial support from the European Research Council (ERC Starting Grant #335078-COLOURATOMS). J.U. acknowledges funding from the Fonds Wetenschappelijk Onderzoek in Flanders (FWO, postdoctoral grant 12I7816N).

Supporting Information Available

Histograms of the particle distributions determined with FESEM; 2D TEM image of the low overpotential catalyst with FFT image; TEM tomography three dimensional reconstruction of synthesized catalysts. This material is available free of charge via the Internet at `http://pubs.acs.org/`.

References

(1) Srinivasan, S. *Fuel Cells: From Fundamentals to Applications*; Springer Science, New York, 2006; p 691.

(2) Lipman, T. E.; Edwards, J. L.; Kammen, D. M. *Energy Policy* **2004**, *32*, 101–125.

(3) Hayden, B. E.; Pletcher, D.; Suchsland, J.-P.; Williams, L. J. *Phys. Chem. Chem. Phys.* **2009**, *11*, 9141–8.

(4) Schäfer, D.; Mardare, C.; Savan, A.; Sanchez, M. D.; Mei, B.; Xia, W.; Muhler, M.; Ludwig, A.; Schuhmann, W. *Anal. Chem.* **2011**, *83*, 1916–1923.

(5) Cheng, N.; Liu, J.; Banis, M. N.; Geng, D.; Li, R.; Ye, S.; Knights, S.; Sun, X. *Int. J. Hydrogen Energy* **2014**, *39*, 15967 – 15974.

(6) Geboes, B.; Mintsouli, I.; Wouters, B.; Georgieva, J.; Kakaroglou, A.; Sotiropoulos, S.; Valova, E.; Armyanov, S.; Hubin, A.; Breugelmans, T. *Appl. Catal., B* **2014**, *150-151*, 249–256.

(7) Alia, S. M.; Larsen, B. a.; Pylypenko, S.; Cullen, D. a.; Diercks, D. R.; Neyerlin, K. C.; Kocha, S. S.; Pivovar, B. S. *ACS Catal.* **2014**, *4*, 1114–1119.

(8) Wang, C.; Chi, M.; Li, D.; Strmcnik, D.; van der Vliet, D.; Wang, G.; Komanicky, V.; Chang, K.-C.; Paulikas, A. P.; Tripkovic, D.; Pearson, J.; More, K. L.; Markovic, N. M.; Stamenkovic, V. R. *J. Am. Chem. Soc.* **2011**, *133*, 14396–403.

(9) Gan, L.; Heggen, M.; O'Malley, R.; Theobald, B.; Strasser, P. *Nano Lett.* **2013**, *13*, 1131–1138.

(10) Baldizzone, C.; Gan, L.; Hodnik, N.; Keeley, G.; Kostka, A.; Heggen, M.; Strasser, P.; Mayrhofer, K. J. J. *ACS Catal.* **2015**, *5*, 5000–5007.

(11) Dubau, L.; Asset, T.; Chattot, R.; Bonnaud, C.; Vanpeene, V.; Nelayah, J.; Maillard, F. *ACS Catal.* **2015**, *5*, 5333–5341.

(12) Xu, C.; Liu, Y.; Hao, Q.; Duan, H. *J. Mater. Chem.A* **2013**, *1*, 13542.

(13) Snyder, J.; Livi, K.; Erlebacher, J. *Adv. Funct. Mater.* **2013**, *23*, 5494–5501.

(14) Snyder, J.; McCue, I.; Livi, K.; Erlebacher, J. *J. Am. Chem. Soc.* **2012**, *134*, 8633–8645.

(15) Bae, J. H.; Han, J.-H.; Chung, T. D. *Phys. Chem. Chem. Phys.* **2012**, *14*, 448–463.

(16) Mahmoud, M. A.; Saira, F.; El-Sayed, M. A. *Nano Lett.* **2010**, *10*, 3764–3769.

(17) Stamenkovic, V. R.; Fowler, B.; Mun, B. S.; Wang, G.; Ross, P. N.; Lucas, C. a.; Marković, N. M. *Science* **2007**, *315*, 493–7.

(18) Chen, H. M.; Liu, R. S.; Lo, M. Y.; Chang, S. C.; Tsai, L. D.; Peng, Y. M.; Lee, J. F. *J. Phys. Chem. C* **2008**, *112*, 7522–7526.

(19) Kibsgaard, J.; Gorlin, Y.; Chen, Z.; Jaramillo, T. F. *J. Am. Chem. Soc.* **2012**, *134*, 7758–7765.

(20) Wu, Y.; Wang, D.; Niu, Z.; Chen, P.; Zhou, G.; Li, Y. *Angew. Chem. Int. Ed.* **2012**, *51*, 12524–12528.

(21) Kleijn, S. E. F.; Lai, S. C. S.; Koper, M. T. M.; Unwin, P. R. *Angew. Chem. Int. Ed.* **2014**, *53*, 3558–3586.

(22) Vanrenterghem, B.; Geboes, B.; Bals, S.; Ustarroz, J.; Hubin, A.; Breugelmans, T. *Appl. Catal., B* **2015**, *181*, 542–549.

(23) Liu, H.; Favier, F.; Ng, K.; Zach, M.; Penner, R. *Electrochim. Acta* **2001**, *47*, 671–677.

(24) Penner, R. M. *J. Phys. Chem. B* **2002**, *106*, 3339–3353.

(25) Burda, C.; Chen, X.; Narayanan, R.; El-Sayed, M. a. *Chem. Rev.* **2005**, *105*, 1025–102.

(26) Cu, C.; Shell, O. C.; One-step, S.; Electrodeposition, C.-a.-f.; Radi, A.; Pradhan, D.; Sohn, Y.; Leung, K. T. *ACS Nano* **2010**, *4*, 1553–1560.

(27) Brülle, T.; Ju, W.; Niedermayr, P.; Denisenko, A.; Paschos, O.; Schneider, O.; Stimming, U. *Molecules* **2011**, *16*, 10059–77.

(28) Durante, C.; Perazzolo, V.; Perini, L.; Favaro, M.; Granozzi, G.; Gennaro, A. *Appl. Catal., B* **2014**, *158-159*, 286–295.

(29) Bayati, M.; Abad, J. M.; Nichols, R. J.; Schiffrin, D. J. *J. Phys. Chem. C* **2010**, *114*, 18439–18448.

(30) Saibuathong, N.; Saejeng, Y.; Pruksathorn, K.; Hunsom, M.; Tantavichet, N. *J. Appl. Electrochem.* **2010**, *40*, 903–910.

(31) Kim, H.; Subramanian, N. P.; Popov, B. N. *J. Power Sources* **2004**, *138*, 14–24.

(32) Mitzel, J.; Arena, F.; Natter, H.; Walter, T.; Batzer, M.; Stefener, M.; Hempelmann, R. *Int. J. Hydrogen Energy* **2012**, *37*, 6261–6267.

(33) Thompson, S. D.; Jordan, L. R.; Forsyth, M. *Electrochim. Acta* **2001**, *46*, 1657–1663.

(34) Kirkendall, E.; Thomassen, L.; Uetegrove, L. *Trans. AIME* **1939**, *133*, 186–203.

(35) Gonzalez, E.; Arbiol, J.; Puntes, V. F. *Science* **2011**, *334*, 1377–1380.

(36) Zhang, Y.; Ma, C.; Zhu, Y.; Si, R.; Cai, Y.; Wang, J. X.; Adzic, R. R. *Catal. Today* **2013**, *202*, 50–54.

(37) Dubau, L.; Lopez-Haro, M.; Durst, J.; Guetaz, L.; Bayle-Guillemaud, P.; Chatenet, M.; Maillard, F. *J. Mater. Chem.A* **2014**, *2*, 18497–18507.

(38) Ustarroz, J.; Altantzis, T.; Hammons, J. a.; Hubin, A.; Bals, S.; Terryn, H. *Chem. Mater.* **2014**, *26*, 2396–2406.

(39) Ustarroz, J.; Gupta, U.; Hubin, A.; Bals, S.; Terryn, H. *Electrochem. Commun.* **2010**, *12*, 1706–1709.

(40) Ustarroz, J.; Hammons, J. A.; Altantzis, T.; Hubin, A.; Bals, S.; Terryn, H. *J. Am. Chem. Soc.* **2013**, *135*, 11550–11561.

(41) Ng, K. H.; Liu, H.; Penner, R. M. *Langmuir* **2000**, *16*, 4016–4023.

(42) Ustarroz, J.; Ke, X.; Hubin, A.; Bals, S.; Terryn, H. *J. Phys. Chem. C* **2012**, *116*, 2322–2329.

(43) Sogaard, M.; Odgaard, M.; Skou, E. M. *Solid State Ionics* **2001**, *145*, 31–35.

(44) Ross, P. N. J.; Markovic, N. M.; Jr, P. N. R. *Surf. Sci. Rep.* **2002**, *45*, 117–229.

(45) Guterman, V. E.; Lastovina, T. a.; Belenov, S. V.; Tabachkova, N. Y.; Vlasenko, V. G.; Khodos, I. I.; Balakshina, E. N. *J. Solid State Electrochem.* **2013**, *18*, 1307–1317.

(46) Zheng, J. N.; He, L. L.; Chen, C.; Wang, A. J.; Ma, K. F.; Feng, J. J. *J. Power Sources* **2014**, *268*, 744–751.

(47) Mayrhofer, K.; Strmcnik, D.; Blizanac, B.; Stamenkovic, V.; Arenz, M.; Markovic, N. *Electrochim. Acta* **2008**, *53*, 3181–3188.

(48) Paulus, U.; Schmidt, T.; Gasteiger, H.; Behm, R. *J. Electroanal. Chem.* **2001**, *495*, 134–145.

(49) Lima, F.; de Castro, J.; Santos, L.; Ticianelli, E. *J. Power Sources* **2009**, *190*, 293–300.

(50) Gasteiger, H. a.; Kocha, S. S.; Sompalli, B.; Wagner, F. T. *Appl. Catal., B* **2005**, *56*, 9–35.

Graphical TOC Entry